

Alleviating Projection-Space Sensitivity in DFT+U via Renormalized U

Manjula Raman¹ and Kenneth Park^{1, a)}

Department of Physics & Astronomy, Baylor University, Waco, Texas 76798-7316, USA

(Dated: 10 March 2026)

Although the DFT+U method significantly improves the description of correlated electronic systems, its accuracy is known to depend strongly on the input parameters including local projection space used for the Hubbard correction. As a result, calculations performed with different projection sizes can yield quantitatively different—and sometimes divergent—results. In this work, we investigate the dependence of the effective Coulomb interaction U_{eff} on projection size using constrained DFT calculations for rutile TiO_2 and $\beta\text{-MnO}_2$. We find that as the projection size increases, the self-consistently calculated U_{eff} decreases significantly—by as much as 33%. This trend is attributed to renormalization of the Coulomb interaction through orbital relaxation and enhanced screening. When U_{eff} values recalculated for each projection size are employed, the results for lattice parameters, electronic structure, and relative phase stability become consistent across different projection sizes. These findings can provide a practical route to alleviate projection-size dependence in DFT+U calculations.

^{a)}Electronic mail: kenneth_park@baylor.edu; <https://physics.artsandsciences.baylor.edu/person/dr-kenneth-t-park>

I. INTRODUCTION

The density functional theory supplemented with Hubbard-correction (DFT+U) is widely used to study systems with strong electron correlation effects^{1,2}. Its popularity stems from the substantial improvements it offers—particularly in predicting electronic structure—while maintaining relatively modest computational cost. However, the accuracy of DFT+U results is highly sensitive to several user-defined input parameters and methodological choices. Among these, the on-site Coulomb energy U and exchange energy J play central roles, as they directly influence the effective electron–electron interactions in solids. This sensitivity has led to widespread practice of tuning U to reproduce experimental observation of selected properties.

Another important consideration is whether to use separate U and J values or the combined parameter $U_{\text{eff}} = U - J$ (with $J = 0$). This choice can significantly affect outcomes. For example, Tompsett *et al.*³ showed that the “full anisotropy” approach—explicitly including both U and J —correctly predicts the antiferromagnetic ground state and the 0.8 eV band gap of β -MnO₂. In contrast, the simplified U_{eff} approach incorrectly favors a ferromagnetic state. They attributed this improvement to a more accurate description of spin polarization in Mn d orbitals, particularly through reducing unphysical spin polarization of bonding states. Similarly, Mellan *et al.*⁴ demonstrated that the correct magnetic ground state and Jahn–Teller distortion in LaMnO₃ are reproduced only when the exchange term J is explicitly included. Yoon *et al.*⁵ further reported that the exchange correction has a stronger influence in Mn³⁺ than in Mn²⁺ in their study of mixed-valent Mn₃O₄.

Beyond the choice of U and J , many studies have noted that the size of the projection sphere and the construction of local orbitals can strongly influence quantitative results—from lattice parameters to electronic structures as well as magnetic ground states^{6–15}. Wang *et al.*⁶ reported substantial discrepancies in DFT+U calculations of MnO and MnO₂ using the U_{eff} scheme across different computational codes. They attributed these differences to variations in the radial extent of Mn $3d$ orbitals defining the Hubbard subspace. In our recent work¹⁵, we systematically demonstrated that the spatial range used for the Hubbard correction alone can lead to strikingly different results in TiO₂. Notably, the optimized lattice parameters exhibit strong sensitivity to the input U , with the lattice constant increasing by as much as 1.8 %. In addition, when the projection space for the Hubbard correction is

chosen too small, even large U values (up to 10 eV) fail to stabilize rutile against anatase, contrary to established literature^{16,17}. These discrepancies arise from the dependence of orbital occupancy on the projection size. The differing orbital occupancy further affects the orbital-dependent potential energy shifts and produces quantitatively distinct electronic structures. Careful consideration is therefore essential for interpreting DFT+U results and extracting meaningful physical insights.

The sensitivity of DFT+U to the size of the local projection space is problematic because this space is not uniquely defined, yet orbital occupations—and thus the Hubbard correction—depends on it. To address this issue, Wang and Jiang¹⁸ reformulated DFT+U using a Thomas–Fermi screening model to determine U , reporting reduced sensitivity to projection size in several oxides. On the other hand, Nawa *et al.*¹⁹ used a linear response theory to show that U_{eff} can decrease by 2-3 eV in an approximately linear fashion for transition metal monoxides as the projection size increases. Using these scaled U_{eff} values, they obtained valence-band structures that varied little despite the large changes in U_{eff} . They attributed this consistency to an approximately linear relationship between U_{eff} and the occupancy of local orbitals.

However, the orbital occupation is only one of the parameters that depend on projection size. The on-site Coulomb repulsion itself— U_{eff} —is the other defining component of the Hubbard correction. Its sensitivity to projection size has not been examined in detail. In this work, we present a systematic investigation of how U_{eff} varies with projection size and the consequence of neglecting or incorporating this dependence. We illustrate these effects using DFT+U calculations for rutile TiO_2 and $\beta\text{-MnO}_2$, two prototypical systems whose structural, electronic, and energetic properties are well known to be sensitive to the size of the Hubbard projection space. These materials are also of broad technological importance, including heterogeneous catalysis, photocatalysis, and energy-storage applications^{20–25}.

II. METHODS AND COMPUTATIONAL DETAILS

A. LAPW and APW+lo approaches

The DFT calculations were performed using the all-electron, full-potential augmented plane wave plus local orbitals (APW+lo) method implemented in the WIEN2k software

package^{26,27}. In this method, the unit cell is divided into non-overlapping muffin-tin (MT) spheres centered at atomic sites and an interstitial region. Inside the MT spheres, the Kohn-Sham wave functions are expanded in spherical harmonics multiplied by radial functions, while in the interstitial region they are represented by plane waves.

The linearized APW (LAPW) basis functions within the atomic spheres are expressed as follows:

$$\psi_{l,m}^{\text{MT}}(r) = A_{l,m}u_l(r, E_l) + B_{l,m}\dot{u}_l(r, E_l) \quad (1)$$

where $u_l(r, E_l)$ is the solution to the radial Schrödinger equation at energy E_l , and $\dot{u}_l(r, E_l)$ is its energy derivative. The coefficients $A_{l,m}$ and $B_{l,m}$ are determined to ensure that the LAPW basis functions match smoothly with the interstitial plane waves, preserving both the function and its derivative at the sphere boundaries.

To improve variational flexibility of the basis set—particularly for semi-core and higher-lying conduction states—the LAPW basis was augmented with local orbitals (lo), forming the APW+lo scheme.²⁸ The local orbitals are defined as

$$\varphi_{l,m}^{\text{lo}}(r) = A_{l,m}^{\text{lo}}u_l(r, E_l^{\text{lo}}) + B_{l,m}^{\text{lo}}\dot{u}_l(r, E_l^{\text{lo}}) \quad (2)$$

and are normalized within the sphere, while vanishing at the MT boundary. These orbitals enhance the description of states not well represented by the standard LAPW basis.

All calculations employed the APW+lo scheme. Core and valence electrons were separated at an energy threshold of -6.0 Ry. For titanium, the $3s$ and $3p$ were treated as semi-core, while the Ti $3d$, $4s$, and O $2s$, $2p$ were treated as valence. Core states were handled fully relativistically via the Dirac–Fock approach, and valence states were treated with a scalar-relativistic approximation. Exchange–correlation effects were described by the Perdew–Burke–Ernzerhof (PBE) functional^{29,30} within the generalized gradient approximation (GGA).

B. Control of Projection Space via Muffin-Tin Radii

In APW+lo calculations, the local projection space is uniquely defined by the muffin-tin sphere. To examine projection-size effects, we systematically varied the MT radius R_{MT} .

For Ti in rutile TiO₂, R_{MT} was increased from 1.91 to 2.00, 2.10, 2.20, and 2.30 bohr radius a_B . To prevent overlap of MT spheres, the oxygen radii were reduced from 1.59 to 1.50, 1.40, and 1.30 a_B ; the latter value was used for Ti $R_{\text{MT}} = 2.20$, and 2.30 a_B . A similar procedure was applied to β -MnO₂, where Mn R_{MT} was varied from 1.90 to 2.00, 2.10, and 2.20 a_B and O R_{MT} was adjusted from 1.55 to 1.48, 1.40, and 1.30 a_B .

The basis-set size of our calculations was controlled through the dimensionless parameter $R_{\text{MT}}K_{\text{Max}}$. To balance accuracy and computational cost, we initially used the Wien2k "precision level 2," corresponding to $R_{\text{MT}}K_{\text{Max}}$ values from 7.00 to 7.22 depending on the chosen MT radii. These values, along with the number of k -points in Brillouin zone and the cutoff g_{max} for the Fourier expansion of the charge density and potential, were subsequently increased during convergence testing. Self-consistency was reached when the total energy converged within 0.000001 Ry and charges within 0.00001. For structural relaxations, atomic forces were converged to below 1 mRy/ a_B .

C. Estimating *ab initio* U_{eff} with constrained DFT

The on-site Coulomb energy was obtained self-consistently using the constrained DFT (cDFT) method proposed by Anisimov and Gunnarsson.^{31,32} In this approach, U_{eff} is interpreted as the energy cost of transferring a localized d - or f - electron from one site to another: $d^n + d^n \rightarrow d^{n+1} + d^{n-1}$. The effective Hubbard parameter is approximated as the lowest-order screened Slater integral F^0 :

$$U_{\text{eff}} = \varepsilon_{3d\uparrow} \left(\frac{n+1}{2}, \frac{n}{2} \right) - \varepsilon_{3d\uparrow} \left(\frac{n+1}{2}, \frac{n}{2} - 1 \right) - \varepsilon_F \left(\frac{n+1}{2}, \frac{n}{2} \right) + \varepsilon_F \left(\frac{n+1}{2}, \frac{n}{2} - 1 \right) \quad (3)$$

where $\varepsilon_{3d\uparrow}(n^\uparrow, n^\downarrow)$ is the spin-up $3d$ eigenvalue for the specified occupancy, and $\varepsilon_F(n^\uparrow, n^\downarrow)$ is the corresponding Fermi energy.

In the original formulation using a linearized MT orbital basis, the hopping integrals between the impurity d states and the rest of the system were set to zero. Because this constraint cannot be applied directly within the LAPW/APW+lo framework, we followed the method proposed by Madsen and Novak²⁸, in which the linearization energy is placed far above the Fermi level to effectively remove the d orbitals from the basis. For TiO₂, $2 \times 2 \times 2$ and $2 \times 2 \times 3$ supercells were constructed using fully optimized lattice parameters, with one

site designated as the impurity. For β -MnO₂, experimental lattice parameters were used to build a $2 \times 2 \times 2$ supercell so that our calculated U_{eff} values could be compared to previously reported results.³ Detailed procedures and convergence tests are provided in Table S1 of the Supplementary Materials.

The magnetic ground state of β -MnO₂ is known to be a helical antiferromagnetic (AFM) with pitch (7/2) along the c axis.^{33–35} For the comparison in the total energy and other properties between AFM and ferromagnetic (FM) configurations, we adopted a simplified collinear antiferromagnetic ordering—the magnetic moments aligned in opposite directions along the body diagonal. This approach has been commonly used in the literature to assess Hubbard-corrected energetics and property calculations in MnO₂^{3,6,36,37}.

III. RESULTS & DISCUSSION

A. Dependence of U_{eff} on Projection Size

Figure 1 shows the self-consistent U_{eff} values for TiO₂ computed at several Ti muffin-tin radii. The value is largest, 4.5 eV at $R_{MT} = 1.91 a_B$. As R_{MT} increases, U_{eff} decreases steadily, reaching 3.0 eV at $R_{MT} = 2.3 a_B$, roughly 67 % of the initial value (Fig. 1(a)). This clear monotonic reduction demonstrates an unmistakable dependence of the effective Coulomb interaction on the projection size.

To determine whether a similar trend appears in other *ab initio* approaches, several literature values obtained via the linear-response theory^{8,42}—a widely used alternative for determining U_{eff} —are compiled in Fig. 1 (b). Two observations emerge. First, U_{eff} tends to be larger when the pseudopotentials include semi-core states into the valence states. For instance, Curnan and Kitchin¹⁷ reported a value of 3.102 eV for rutile using standard PAW pseudopotentials with PBE (open squares). Including p semi-core states increased this value to 4.773 eV, and including s semi-core states raised it further to 6.030 eV. They noted that the standard PAW-pseudopotentials result agrees well with the value reported by Mattioli and Filippone *et al.*—3.23 eV—obtained with standard ultrasoft pseudopotentials (grey open triangle).^{39,43} On the other hand, the U_{eff} value obtained with p -inclusive PAW pseudopotentials closely matched the 4.95 eV reported by Xu *et al.* using a pseudopotential constructed from GBRV library (blue open circle)⁴⁰. They further observed a similar trend

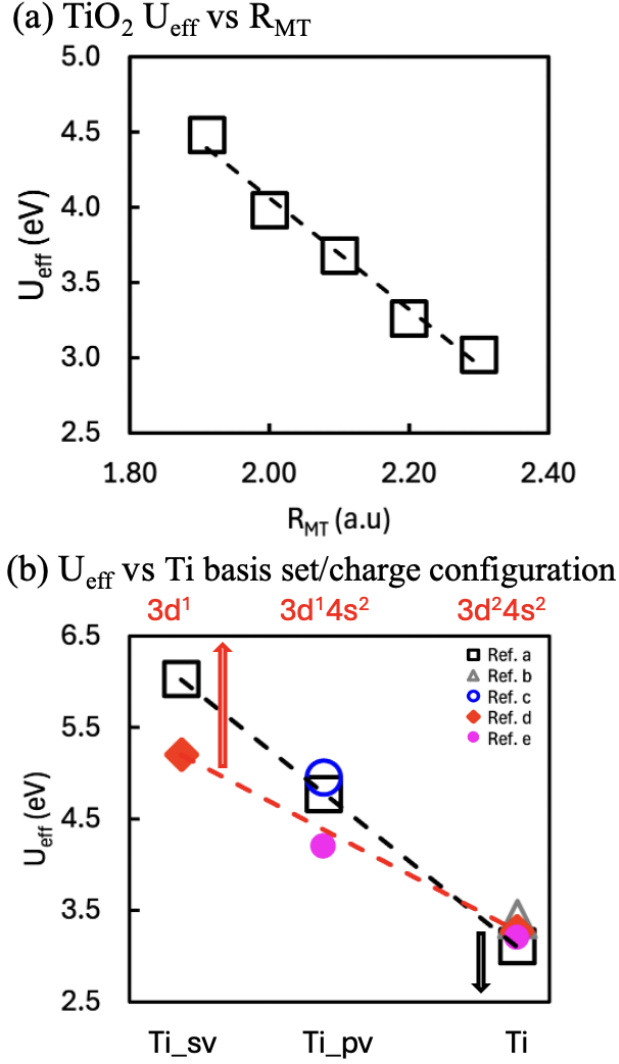


FIG. 1. (a) the self-consistently determined on-site Coulomb interaction parameter U_{eff} as a function of Ti muffin-tin radius R_{MT} for TiO_2 using the cDFT method. (b) U_{eff} values obtained using linear-response theory for rutile TiO_2 in literature plotted against different Ti valence sets (open symbols for bottom and left axes) and charge configurations (filled symbols for top and left axes). Ti , Ti_{pv} , and Ti_{sv} represent standard, p - and s -semicore inclusive pseudopotentials, respectively. The dashed lines are only to guide the eyes. References a:¹⁷, b:³⁸, c:³⁹, d:⁴⁰, e:⁴¹.

of semi-core inclusive pseudopotentials producing larger U_{eff} for anatase as well.

Second, U_{eff} also depends strongly on the ionic configuration used to generate the pseudopotential. Orhan and O'Regan *et al.*³⁸ employed a minimum-tracking variant of linear response scheme with LDA functional to evaluate U_{eff} . They reported values of ~ 3.27 eV for rutile and anatase when using the pseudopotential constructed from a neutral Ti con-

figuration (red filled diamonds in Fig. 1 (b)). However, switching to a Ti^{3+} reference state ($3d^1$) increased U_{eff} to 5.20 eV. They attributed the larger U_{eff} to the more localized Ti $3d$ subspace represented by this pseudopotential. Likewise, Camellone *et al.*⁴¹ obtained $U_{\text{eff}} = 3.2$ eV for rutile TiO_2 using a PAW-based pseudopotential generated from a neutral atom configuration with PBE (pink filled circles). When using a pseudopotential constructed from a Ti^{1+} reference state ($3d^1 4s^2$), their calculated U_{eff} value increased to 4.2 eV. They also noted a similar sensitivity in FeO, where U_{eff} increases from 4.6 eV for a pseudopotential created from a neutral Fe atom, to 7.8 eV for one generated from an Fe^{2+} reference state in the LDA+U calculations employing a linear combination of atomic orbital basis⁸.

Although the absolute magnitudes of U_{eff} vary among the linear-response and the constrained-occupancy approaches, the observed dependencies on pseudopotential valence configuration and charge state closely mirror the R_{MT} dependence we observed (Fig. 1 (a)). The consistency across different computational frameworks—whether using APW+lo or pseudopotential methods, and whether applying cDFT or linear response theory—suggests that the results unlikely originate from any specific methodology. Instead, it points to a common underlying physical cause that all approaches are capturing. Since the size of Hubbard projection in this study is independently controlled by a single parameter—the muffin-tin radius, it is reasonable to conclude that the sensitivity of U_{eff} on the differences in pseudopotential construction also stems from the spatial extent of the localized d subspace.

To understand how the size of the projection space could influence U_{eff} , we examined the spatial characteristics of the localized orbitals with different projection sizes. Figure 2 shows the radial probability distribution $r^2\rho(r)$ of the Ti d orbitals in rutile TiO_2 , calculated using the PBE functional, for three different values of R_{MT} . As R_{MT} increases, the shape of the Ti d orbitals evolves noticeably, with a more pronounced tail extending outward for larger projection spaces. The mean radius of the d orbitals $\langle r \rangle = \int_0^{R_{\text{MT}}} r^2 dr \rho(r) r$ provides a useful quantitative measure of this spatial extent. As R_{MT} increases from 1.91 to 2.30 a_B , the $\langle r \rangle$ increases from 0.92 a_B to 1.00 a_B , respectively, indicating a clear spatial dilation of the localized orbitals.

This increase in spatial extent directly affects the computed on-site Coulomb interaction U_{eff} . It is important to recall that U_{eff} is a renormalized quantity representing the energy cost of transferring a localized electron from one site to another.^{31,44} This energy cost includes screening by other valence electrons such as the $4s$ and $4p$ electrons in $3d$ transition metals.

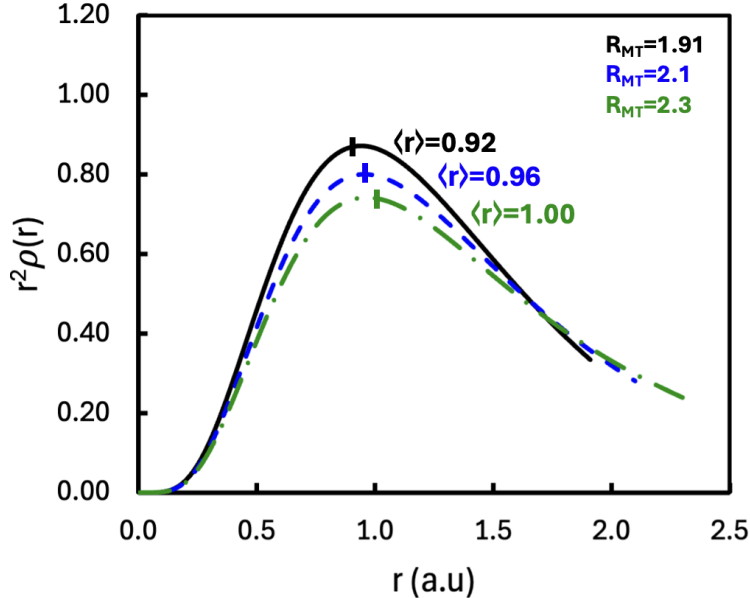


FIG. 2. Radial probability distribution function of Ti d orbitals in rutile TiO_2 calculated for three different muffin-tin radii, using the PBE exchange-correlation functional.

Such screening reduces U_{eff} in the solid much smaller than the unscreened Slater integral of the corresponding atom.²⁸

Solovyev and Dederichs⁴⁵ further highlighted the importance of orbital relaxation in understanding on-site Coulomb interaction U_{eff} . They showed that the U_{eff} of transition metal impurities in Rb varies significantly with electronic configuration: for $3d$ impurities, the value is about 30 % larger in the divalent configuration than in the monovalent one. They attributed this dependence to changes in relaxation and screening as the localized orbitals become more or less contracted—an effect that mirrors the sensitivity of U_{eff} on the atomic number for a fixed valence configuration.

We propose that similar relaxation and screening mechanisms are responsible for the dependence of U_{eff} on the projection space. As the projection space expands, the mean separation between the localized electrons increases accordingly. The *ab initio* calculated U_{eff} therefore decreases to reflect the reduced on-site Coulomb repulsion. Consequently, applying a single fixed U_{eff} across different projection sizes is not justified. Instead, U_{eff} should be recalculated for each chosen projection space so that the Hubbard interaction term correctly incorporates the renormalized Coulomb interaction.

B. Calculated Properties of TiO₂ and MnO₂ using Renormalized U_{eff} Scheme

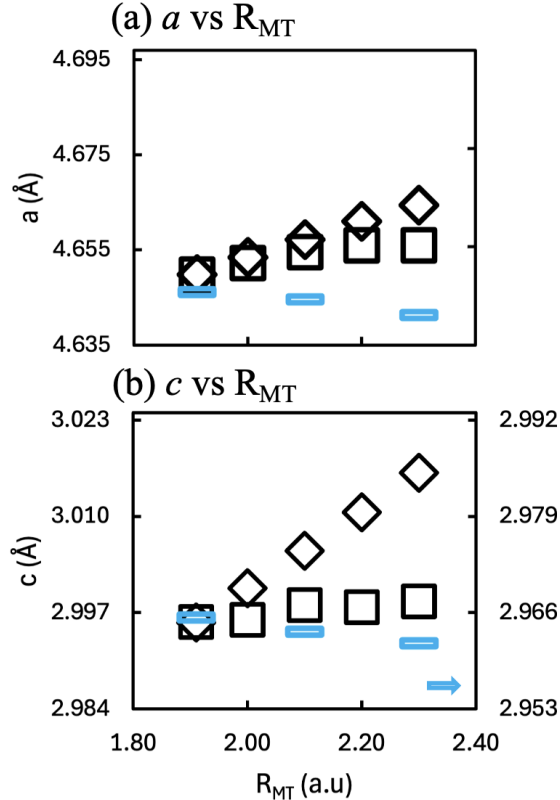


FIG. 3. Calculated lattice parameters (a) a and (b) c of TiO₂ as a function of Ti muffin-tin radius with two computational schemes. For fixed U_{eff} scheme (diamond markers), U_{eff} values are constant and fixed at 4.5 eV. For renormalized U_{eff} scheme (square markers), U_{eff} values from the Fig.1 are used at each R_{MT} . As for the reference values, the lattice parameters computed without the Hubbard correction (light blue) are also shown for comparison.

Figure 3 compares the lattice constants a and c as functions of Ti R_{MT} computed using two schemes: (1) U_{eff} fixed to 4.5 eV applied for all R_{MT} values, and (2) a renormalized U_{eff} determined individually at each R_{MT} from Fig. 1. Under the fixed- U scheme (diamonds), the lattice parameter c expands by about 0.7 % as R_{MT} increases from 1.91 to 2.3 a_B while the lattice parameter a shows a smaller increase of approximately 0.3 %. This asymmetrical lattice expansion has been noted previously.¹⁵ It has been attributed to the uneven bond lengths in rutile structure combined with increased Ti ionic character especially at larger R_{MT} , arising from greater depletion of the d -orbital population (n_d) (Table S2). In contrast, structural optimization using the renormalized U_{eff} values for each projection space yields

lattice parameters that remain largely consistent across different R_{MT} values (squares). Although the resulting lattice constants are slightly larger than those obtained using PBE alone (blue bars), as expected, they vary no more than 0.006 Å across the full range of R_{MT} . Their consistency is comparable to the PBE reference without the Hubbard correction.

Despite the substantial improvement afforded by the renormalized U_{eff} scheme, the lattice parameters especially calculated at larger R_{MT} values exhibit some residual sensitivity to the projection size. The exact origin of this deviation is unclear. Solovyev suggested that, in certain cases, the presence of additional electrons or particular electronic configurations can counteract the expected trend, causing U_{eff} to remain constant or even increase. Another possibility is that, as the difference between the Ti and O in muffin-tin radii grows, the quality of the local basis set expansion gradually deteriorates, reducing consistency with the rest of the data.

Next, we examined the electronic structure obtained using the two U_{eff} schemes. Figure 4 (a) and (b) show the projected density of states (PDOS) for rutile TiO_2 in the valence- and conduction-band regions, computed with a fixed $U_{\text{eff}} = 4.5$ eV and with renormalized U_{eff} values, respectively. Under the fixed U_{eff} scheme, the band gap remains nearly constant, increasing only slightly from 2.37 to 2.40 eV as Ti R_{MT} increases. With the renormalized U_{eff} , the band gap decreases modestly from 2.37 to 2.19 eV (left panels). This overall weak dependence on projection-space size can be attributed in part to the O p character dominating the top of the valence band. In addition, the Ti t_{2g} states that form the bottom of the conduction band are nearly empty and therefore exhibit minimal sensitivity to changes in orbital occupancy.

In contrast to the band gap, the crystal field splitting (CFS) between the t_{2g} and e_g orbitals in the conduction band is more sensitive to the U_{eff} scheme and displays markedly different trends. With a fixed $U_{\text{eff}} = 4.5$ eV, the CFS decreases by about 0.3 eV—from 2.03 to 1.74 eV—as R_{MT} increases (Fig. 4(c)). This reduction arises from uneven shifts of the t_{2g} and e_g states. They are driven by the occupancy dependence of the Hubbard orbital potential, with the bonding e_g orbitals being particularly sensitive on R_{MT} values¹⁵. Although the magnitude of this reduction is modest for a U_{eff} of moderate strength, using a fixed U_{eff} value that is too large can produce unrealistically small CFS values.^{15,16,46} On the other hand, the renormalized U_{eff} scheme yields a nearly constant CFS, varying only from 2.03 to 1.94 eV, owing to the more consistent shifts of the t_{2g} and e_g manifolds across

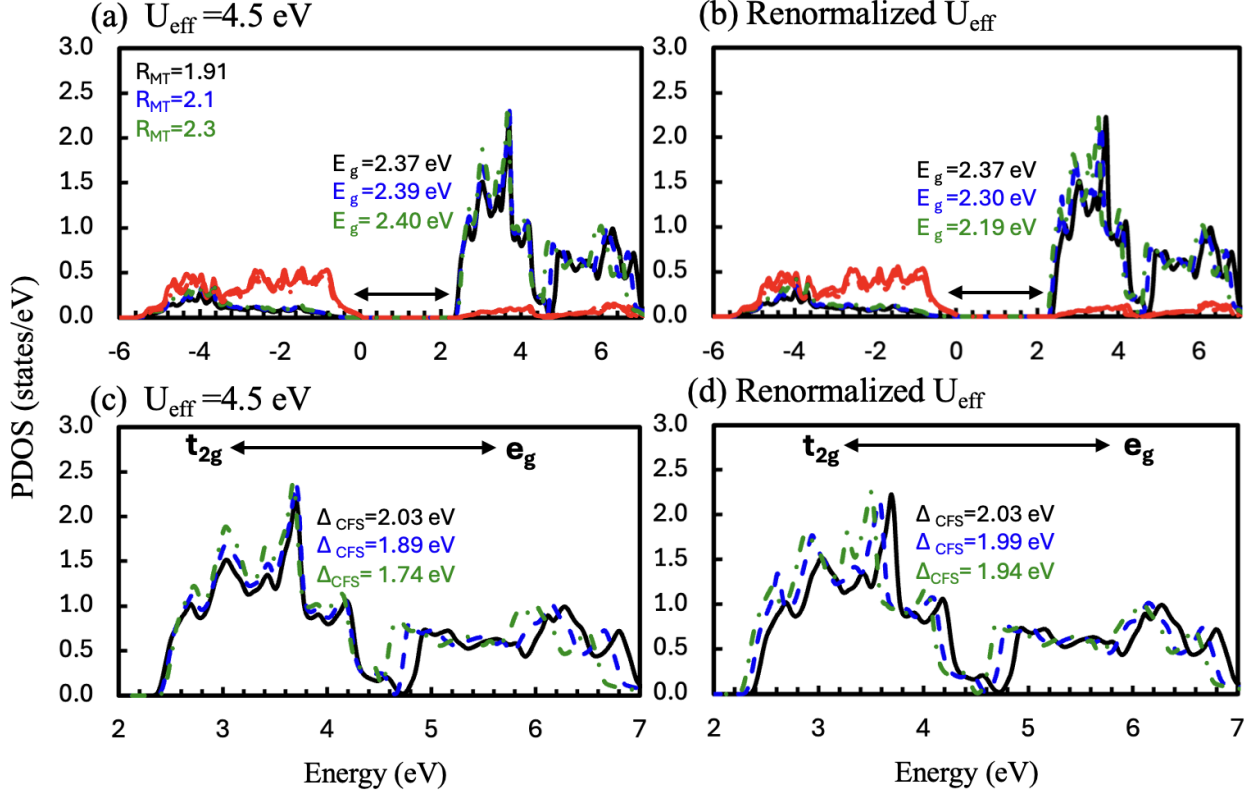


FIG. 4. Projected density of states (PDOS) for Ti *d* and O *p* orbitals in rutile TiO₂ using (a) a single fixed $U_{\text{eff}} = 4.5$ eV and (b) renormalized values U_{eff} for different Ti R_{MT} : 1.91 (solid black), 2.1 (dashed blue), and 2.3 (dash-dotted green) a_B . The PDOS for O 2*p* is in red with the same line patterns. (c) and (d) panels contrast the difference in the calculated CFS between the two different schemes.

different projection sizes (Fig. 4(d)).

To examine whether the renormalized U_{eff} scheme also improves DFT+U calculations for systems with different *d*-electron occupancies and magnetic properties, we investigated the isostructural oxide β -MnO₂. The U_{eff} values for MnO₂ show the same characteristic trend with increasing R_{MT} ; they decrease from 5.6 eV at $R_{\text{MT}} = 1.90 a_B$ to 4.2 eV at $R_{\text{MT}} = 2.20 a_B$ (Fig. 5(a) and Table S3 in Supplementary Materials). This approximately 25 % reduction reflects the same renormalization effect—relaxation and screening of Mn *d* orbitals—as observed in TiO₂. Tompsett *et al.*³ reported $U_{\text{eff}} = 5.50$ eV using Wien2k, presumably at $R_{\text{MT}} = 2.01 a_B$ and employing a similar cDFT methodology. Their value is about 0.3 eV higher than ours (5.2 eV at $R_{\text{MT}} = 2.00 a_B$), though the limited details provided for their computational setup make this small discrepancy difficult to fully resolve.

Nevertheless, despite these minor differences, the strong sensitivity of U_{eff} to the radial extent of the projection space is clearly demonstrated.

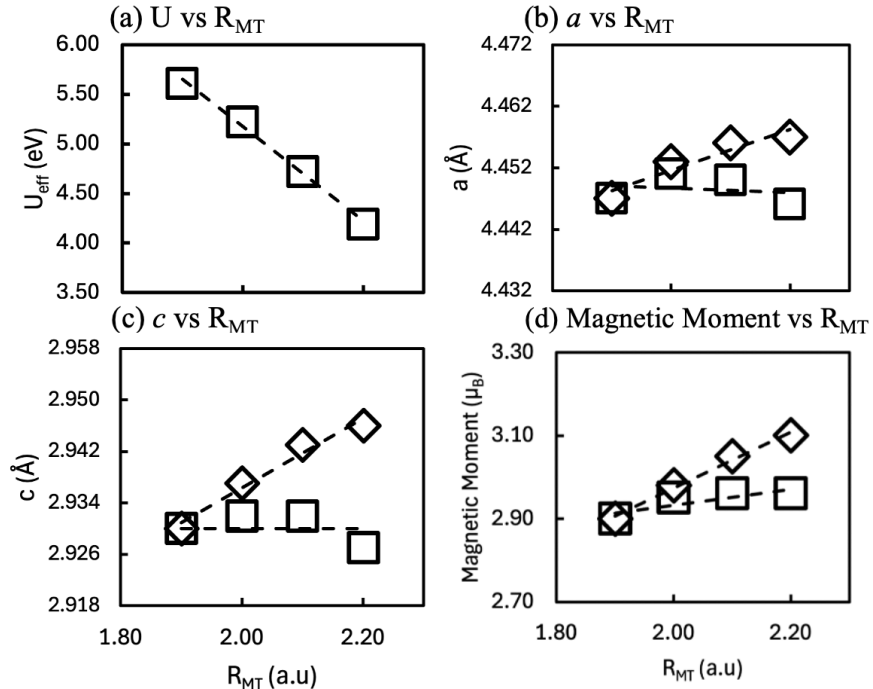


FIG. 5. (a) Self-consistently determined U_{eff} at selected Mn muffin-tin radii (R_{MT}), (b) and (c) the calculated lattice parameters a and c (d) the magnetic moment as a function of Mn R_{MT} for β - MnO_2 in AFM ordering, respectively. In the panels (b) through (d), diamond markers correspond to the results using the fixed U_{eff} value of 5.6 eV, and square markers to those obtained under the renormalized U_{eff} scheme. Dashed lines are guides to the eye.

Our results are consistent with the sensitivity of U_{eff} to projection space in β - MnO_2 , previously hinted by Mahajan *et al.*³⁷ in their study using pseudopotentials constructed from GBRV with PBEsol exchange-correlational functional. They reported that U_{eff} for β - MnO_2 varies by roughly 1.4–2.2 eV across different magnetic configurations when switching from non-orthogonalized atomic orbitals (NAO) to orthogonalized atomic orbitals (OAO). For example, U_{eff} values of 4.93 eV (FM) and 4.67 eV (A1-AFM) obtained using NAOs increased to 7.08 eV and 6.34 eV, respectively when OAOs were used. Because orbital orthogonalization—especially via Löwdin’s symmetric scheme—tends to contract the radial extent of the localized orbitals, this strong dependence of U_{eff} can be interpreted as another manifestation of renormalized Coulomb interaction.

The choice between fixed and renormalized U_{eff} schemes strongly influences structural and magnetic responses to changes in projection space. Using a fixed $U_{\text{eff}} = 5.6$ eV at $R_{\text{MT}} = 1.90 a_B$, structural optimization yields the lattice parameters of $a = 4.447 \text{ \AA}$ and $c = 2.930 \text{ \AA}$ for the AFM configuration (Fig. 5(b) and (c)). Increasing the projection size to $R_{\text{MT}} = 2.20 a_B$ leads to larger lattice constants of 4.457 \AA and 2.946 \AA , respectively (diamonds). In contrast, applying renormalized U_{eff} values at each R_{MT} keeps the lattice constants nearly unchanged, demonstrating the reduced sensitivity to the projection-space size when the renormalization is properly accounted for (squares). The magnetic properties show a similarly contrasting behavior. Under the fixed U_{eff} scheme, the Mn magnetic moment within the MT sphere increases from $2.90 \mu_B$ to $3.10 \mu_B$ as R_{MT} grows (Fig. 5(d)). Renormalized U_{eff} clearly suppresses this trend, stabilizing the magnetic moment across MT radii.

The effects of the fixed and renormalized U_{eff} schemes on the spin-resolved Mn d and O p PDOS are shown in Figure 6. Under both schemes using $R_{\text{MT}} = 1.90 a_B$, the pronounced peaks between -8 and -5 eV correspond primarily localized t_{2g} orbitals of majority-spin (solid blue line). The sharp feature near -5.5 eV is identified as the $d_{x^2-y^2}$ orbital. This feature arises an octahedral distortion associated with the O-Mn-O bond angle in the equatorial plane to $\sim 80^\circ$ according to Tompsett *et al.*³ The peaks around 2 eV above the Fermi energy originate from the e_g states of majority spin. The broad overlap between e_g orbitals and O p states (red) in the valence band region—more clearly visible with $R_{\text{MT}} = 2.2 a_B$ (Fig. S1 in Supplementary Materials) indicates strong Mn–O covalency. Minority-spin t_{2g} and e_g orbitals lie above E_F and remain largely unoccupied (light blue).

Increasing the muffin-tin radius $R_{\text{MT}} = 2.20 a_B$ while keeping $U_{\text{eff}} = 5.6$ eV raises the minority-spin t_{2g} levels by approximately 0.19 eV (green dashed line), indicating reduced hybridization (Fig. 6 (a)). In contrast, under the renormalization scheme, these orbitals shift downward by about 0.26 eV (Fig. 6 (b)). At the same time, the majority-spin t_{2g} bands broaden toward higher energy, strengthening Mn–O overlap. Quantitative analysis of orbital charges and net spin occupations supports this interpretation (Table S4 in the Supplementary Materials). The occupancy in minority-spin t_{2g} increases by 32 % as R_{MT} grows from 1.90 to 2.20 a_B under the renormalized U_{eff} scheme, whereas it increases only by 12 % when using the fixed $U_{\text{eff}} = 5.6$ eV. These markedly different occupancies at $R_{\text{MT}} = 2.20 a_B$ arise from the differing strengths of on-site Coulomb potentials; the fixed U_{eff} scheme overestimates this potential at larger projection size, suppressing orbital occupancy and thereby

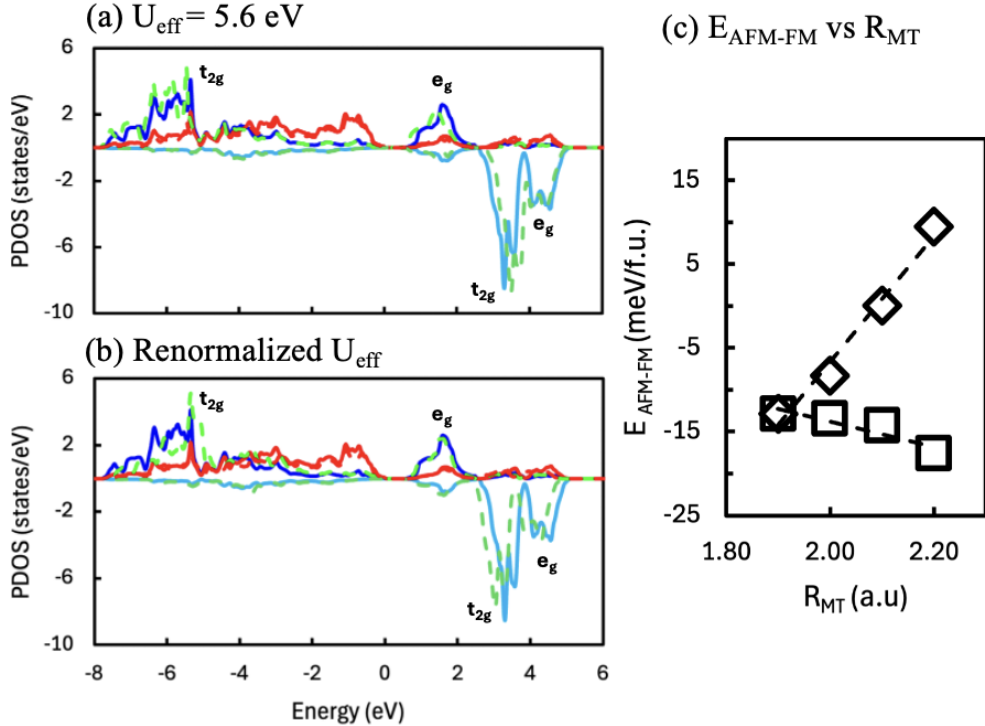


FIG. 6. PDOS for Mn 3d and O 2p orbitals in β -MnO₂ using (a) the fixed $U_{\text{eff}} = 5.6$ eV and (b) renormalized U_{eff} values for two Mn $R_{\text{MT}} = 1.90$ and 2.20 a_B . For $R_{\text{MT}} = 1.90$ a_B , PDOS are plotted in solid lines with Mn majority- and minority-spin states in dark and light blue, respectively as well as the O 2p in red. For $R_{\text{MT}} = 2.20$ a_B , PDOS are plotted in dashed lines with the same color scheme. (c) The total energy difference between AFM and FM configurations ($E_{\text{AFM}} - E_{\text{FM}}$) as a function of Mn R_{MT} calculated with the two schemes: using the fixed $U_{\text{eff}} = 5.6$ eV (diamonds) and renormalized U_{eff} values (squares). The dashed line are only to guide the eyes.

reducing hybridization. Ignoring the renormalization therefore leads to systematically weakened Mn-O hybridization at larger R_{MT} .

The weakened hybridization between Mn d -O p has previously been invoked to explain the AFM-to-FM transition that occurs as U_{eff} increases. For example, Crespo and Seriani⁴⁷ examined a range of AFM and FM configurations in a Hubbard-corrected DFT study of α -MnO₂. They found that the FM ordering becomes energetically favored when $U_{\text{eff}} \geq 2$ eV, whereas AFM ordering is correctly predicted for smaller values ($U_{\text{eff}} \leq 1.6$ eV). They attributed the stabilization of FM ordering to the weakening of AFM superexchange mediated by O p -orbitals, following a simplified argument consistent with the Goodenough-Kanamori-

Anderson rules^{48–51}. In particular, they proposed the reduced hybridization between Mn d states and O p_z orbitals—arising from sp^2 -like mixing—diminishes AFM coupling and favors FM alignment.

An analogous AFM-to-FM transition is observed in our calculations as R_{MT} increases from 1.90 to 2.20 a_B when using the fixed $U_{\text{eff}} = 5.6$ eV (Fig. 6 (c)). At $R_{\text{MT}} = 1.90$ a_B , AFM ordering is preferred by approximately -13 meV, but this preference steadily diminishes and ultimately reverses, yielding a $+9$ meV destabilization over FM ordering at $R_{\text{MT}} = 2.20$ a_B (diamonds). In contrast, calculations employing the renormalized U_{eff} scheme consistently predict an AFM ground state across the entire range of R_{MT} values, with no transition to FM (squares). This behavior underscores the importance of using projection-space-dependent U_{eff} values to avoid artificial magnetic instabilities.

There appears to be a clear equivalence between the effects of enlarging the projection space at a fixed U_{eff} and increasing U_{eff} at a fixed projection size. For β -MnO₂, Wang *et al.*⁶ reported that FM ordering becomes favored when the U_{eff} exceeds about 5 eV, provided a sufficiently large muffin-tin radius—mirroring our observation of an AFM-to-FM transition at larger R_{MT} when a fixed U_{eff} is used. Franchini *et al.*³⁶ likewise found that increasing U_{eff} from 3 to 6 eV leads to an expansion of the unit-cell volume and an increase in magnetic moment from 2.93 μ_B to 3.34 μ_B . These trends closely match the lattice expansion and enhanced magnetic moments we observe as R_{MT} increases (Fig. 5 (b) through (d)). A similar correspondence is seen in TiO₂, where the increase in lattice parameters with larger R_{MT} under a fixed $U_{\text{eff}} = 4.5$ eV (Fig. 3) parallels the behavior reported when U_{eff} is varied at constant projection size.^{15,16} Likewise the dependence of crystal-field splitting on R_{MT} (Fig. 4) closely resembles its sensitivity to U_{eff} at fixed projection size.^{15,16,46}

C. Dependence of Total Energy on Projection Space

Further insight into the origin of the differing behaviors produced by the fixed and normalized U_{eff} schemes can be obtained by examining the total-energy dependence on R_{MT} . Figure 7 (a) shows the total energies of MnO₂ calculated at various R_{MT} values using the fixed $U_{\text{eff}} = 5.6$ eV (diamonds) and the renormalized values (squares), for both AFM (red) and FM (black) configurations. At $R_{\text{MT}} = 1.90$ a_B , the AFM configuration is slightly lower in energy than the FM configuration. Under the fixed U_{eff} scheme, total energies of both

AFM and FM states decrease slightly as R_{MT} increases; however, the FM energy decreases more rapidly, ultimately reversing the relative stability of the two magnetic states.

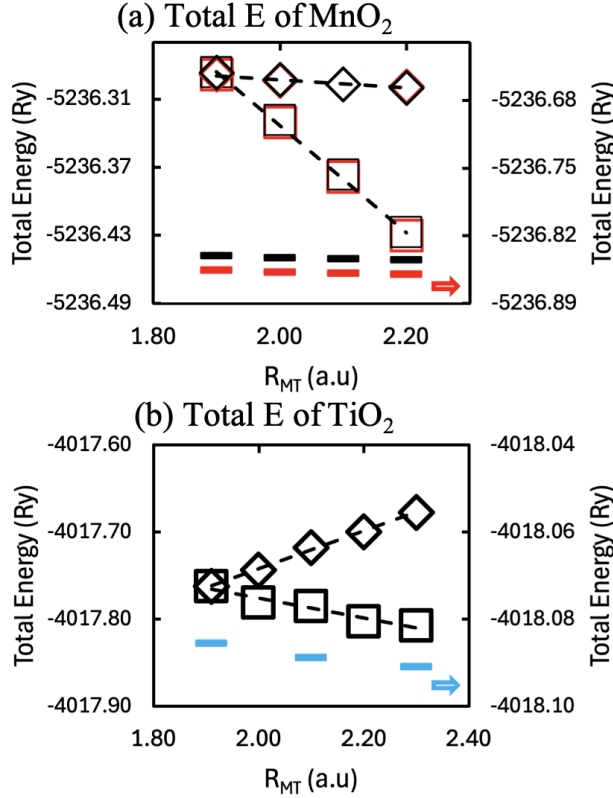


FIG. 7. Comparison of the total energy as a function of R_{MT} between the fixed (diamonds) and renormalized U_{eff} (squares) schemes in (a) the AFM (red) and FM (black) configurations for MnO_2 and (b) for TiO_2 . Under the fixed U_{eff} scheme, the values of 5.6 and 4.5 eV are used for MnO_2 and TiO_2 calculations, respectively. Also shown are the total energy calculations without the Hubbard correction (bars).

In contrast, when renormalized U_{eff} values are used, the total energies of the AFM and FM configurations decrease at nearly the same rate with increasing R_{MT} . As a result, the energy difference between the two magnetic states remains essentially constant across the entire projection-space range, and the AFM ground state is preserved. Notably, the overall decrease in total energy is more pronounced under the renormalized U_{eff} scheme than under the fixed scheme. For TiO_2 (Fig. 7 (b)), the behavior is reversed: the total energy obtained with the renormalized U_{eff} decreases only moderately as R_{MT} increases (squares), whereas the total energy computed using the fixed $U_{\text{eff}} = 4.5$ eV rises sharply with increasing projection

size (diamonds).

For both MnO_2 and TiO_2 , calculations performed with the PBE functional alone show no significant dependence of the total energy on R_{MT} (bars in Fig. 7 (a) & (b)). This indicates that the strong dependence observed in the DFT+U calculations arises primarily from the Hubbard correction term. The contrasting responses of the total energy as a function of R_{MT} can be understood by examining the Hubbard energy contribution $E[n(\mathbf{r})] = \frac{U_{\text{eff}}}{2}n(\mathbf{r})(1 - n(\mathbf{r}))$. Using the Hellmann–Feynman theorem, following the approach of Solovyev and Dederichs⁴⁵, the dependence of the interaction energy on the projection size R through both n and U_{eff} can be expressed as

$$\frac{\partial E}{\partial R} = U_{\text{eff}} n\left(\frac{1}{2} - n\right) \frac{\partial n}{\partial R} + \frac{n(1 - n)}{2} \frac{\partial U_{\text{eff}}}{\partial R} \quad (4)$$

In the fixed U_{eff} scheme, the second term is effectively neglected by assuming $\frac{\partial U_{\text{eff}}}{\partial R} = 0$. Because $\frac{\partial n}{\partial R}$ is generally positive, the sign of the first term is determined by the occupancy of the d -orbitals. In MnO_2 , the combined spin-up and spin-down occupancy $n = n_{\uparrow} + n_{\downarrow}$ exceeds one half (Table S5), resulting in a negative first term with $n(\frac{1}{2} - n) < 0$, and thus a decreasing total energy with increasing R_{MT} (diamonds in Fig. 7 (a)). In TiO_2 , the d -orbitals are less than half-filled, so $n(\frac{1}{2} - n) > 0$ (Table S2). This leads to a monotonically increasing total energy with increasing projection size, as observed in Fig. 7(b) (diamonds).

Under the renormalized U_{eff} scheme, the second term of Eq. 4 is no longer neglected. This term is generally negative, since $\frac{\partial U_{\text{eff}}}{\partial R} < 0$, reflecting the weakening of the Coulomb repulsion with increasing projection size, as shown in Figures 5 (a) and 1 (a) for MnO_2 and TiO_2 , respectively. For MnO_2 , this negative second term reinforces the already decreasing trend of the total energy (squares in Fig. 7 (a)). In contrast, for TiO_2 , the negative second term competes against the positive contribution from the first term of Eq. 4, resulting in a more moderate decrease in total energy (squares in Fig. 7 (b)).

Finally, the insights from this study also clarify the rationale behind the scaled- U_{eff} approach proposed by Nawa *et al.*¹⁹. The reduction of 2–3 eV in U_{eff} reported for MnO , FeO , CoO , and NiO can be understood as manifestations of the same renormalization of the Coulomb interaction as the projection space is varied. By using these scaled U_{eff} values, they achieved more accurate and consistent assessments of the on-site Coulomb interaction across different projection sizes. In avoiding the systematic overestimation inherent in a fixed U_{eff} scheme, their method yielded electronic structures that remain consistent regardless of the

chosen projection space.

IV. CONCLUSIONS

We have addressed the long-standing sensitivity of the DFT+U method to the size of the local projection space used to apply the Hubbard correction. Using all-electron APW+lo calculations combined with constrained DFT, we quantified how the effective Coulomb interaction parameter (U_{eff}) changes with muffin-tin radius (R_{MT}) in rutile TiO_2 and $\beta\text{-MnO}_2$. We find that U_{eff} decreases substantially—by up to 33 %—as the projection regions expands. The behavior aligns with previous findings across a variety of systems and computational approaches, and arises from the radial extent of localized orbitals together with relaxation and enhanced screening effects. These results reinforce that U_{eff} is a renormalized quantity intrinsically linked to its projection space.

Using a properly renormalized Hubbard U_{eff} for each projection space yields consistent lattice parameters, crystal-field splittings, and relative phase stabilities—independent of the projection space. In contrast, applying a single fixed U_{eff} across different projection sizes neglects this renormalization and results in strong, unphysical sensitivity to the projection space. This sensitivity parallels the variations produced by changing U_{eff} within a fixed projection space and reflects inaccurate treatment of onsite Coulomb interactions within the DFT+U framework. Adopting projection-size-dependent U_{eff} values mitigates these discrepancies and enables more robust, transferable predictions. Overall, a properly renormalized Hubbard U_{eff} provides a practical path for improving the reliability of DFT+U for strongly correlated systems with localized d or f electrons.

V. ACKNOWLEDGEMENTS

The authors are grateful for insightful and stimulating discussions with P. Blaha. M.R. is thankful for the travel support from the Department of Physics and Astronomy and the School of Graduate Studies at Baylor University. The authors acknowledge C. Bell at the High Performance Computing Center of Baylor University for technical support.

VI.

REFERENCES

- ¹V. I. Anisimov, F. Aryasetiawan, and A. I. Lichtenstein. First-Principles Calculations of the Electronic Structure and Spectra of Strongly Correlated Systems: The LDA+U Method. *Journal of Physics: Condensed Matter*, 9(4):767–808, 1997.
- ²B. Himmetoglu, A. Floris, S. de Gironcoli, and M. Cococcioni. Hubbard-Corrected DFT energy functionals: The LDA+U description of correlated systems. *International Journal of Quantum Chemistry*, 114(1):14–49, 2014.
- ³D. A. Tompsett, D. S. Middlemiss, and M. S. Islam. Importance of anisotropic Coulomb interactions and exchange to the band gap and antiferromagnetism of β -MnO₂ from DFT+U. *Physical Review B*, 86(20):205126, 2012.
- ⁴T. A. Mellan, F. Corà, R. Grau-Crespo, and S. Ismail-Beigi. Importance of anisotropic Coulomb interaction in LaMnO₃. *Physical Review B*, 92(8):085151, 2015.
- ⁵S. Yoon, S. Lee, S. Pang, M. Kim, and Y.-K. Kwon. Role of anisotropic Coulomb interactions in the superexchange coupling of mixed-valent Mn₃O₄. *Physical Review B*, 104(3):035158, 2021.
- ⁶Y.C. Wang, Z.H. Chen, and H. Jiang. The local projection in the density functional theory plus U approach: A critical assessment. *The Journal of Chemical Physics*, 144(14), 2016.
- ⁷Zi Wang, Casey Brock, Amina Matt, and Kirk H. Bevan. Implications of the DFT+U method on polaron properties in energy materials. *Physical Review B*, 96(12):125150, 2017.
- ⁸WE Pickett, SC Erwin, and EC Ethridge. Reformulation of the LDA+U method for a local-orbital basis. *Physical Review B*, 58(3):1201, 1998.
- ⁹S. Fabris, G. Vicario, G. Balducci, S. de Gironcoli, and S. Baroni. Electronic and Atomistic Structures of Clean and Reduced Ceria Surfaces. *The Journal of Physical Chemistry B*, 109(48):22860–22867, 2005.
- ¹⁰C Tablero. Representations of the occupation number matrix on the LDA/GGA+U method. *Journal of Physics: Condensed Matter*, 20(32):325205, 2008.
- ¹¹Grégory Geneste, Bernard Amadon, Marc Torrent, and Guilhem Dezanneau. DFT+U Study of Self-Trapping, Trapping, and Mobility of Oxygen-Type Hole Polarons in Barium

- Stannate. *Physical Review B*, 96(13):134123, 2017.
- ¹²Robinson Outerovitch and Bernard Amadon. Electronic interaction U_{pp} on oxygen p orbitals in oxides: Role of correlated orbitals on the example of UO_2 and TiO_2 . *Physical Review B*, 107(23):235126, 2023.
- ¹³Seong-Geon Park, Blanka Magyari-Köpe, and Yoshio Nishi. Electronic correlation effects in reduced rutile TiO_2 within the LDA+U method. *Physical Review B*, 82(11):115109, 2010.
- ¹⁴Hyowon Park, Andrew J Millis, and Chris A Marianetti. Density Functional versus Spin-Density Functional and the Choice of Correlated Subspace in Multivariable Effective Action Theories of Electronic Structure. *Physical Review B*, 92(3):035146, 2015.
- ¹⁵K. Park, M. Raman, A.J. Olatunbosun, and J. Pohlmann. Revisiting DFT+U calculations of TiO_2 and the effect of the local-projection size. *AIP Advances*, 14(6), 2024.
- ¹⁶Arroyo-de Dompablo, A Morales-García, M Taravillo, et al. DFT+U Calculations of Crystal Lattice, Electronic Structure, and Phase Stability under Pressure of TiO_2 Polymorphs. *The Journal of chemical physics*, 135(5), 2011.
- ¹⁷Matthew T Curnan and John R Kitchin. Investigating the Energetic Ordering of Stable and Metastable TiO_2 Polymorphs Using DFT+U and Hybrid Functionals. *The Journal of Physical Chemistry C*, 119(36):21060–21071, 2015.
- ¹⁸Yue-Chao Wang and Hong Jiang. Local screened Coulomb correction approach to strongly correlated d-electron systems. *The Journal of Chemical Physics*, 150(15), 2019.
- ¹⁹Kenji Nawa, Toru Akiyama, Tomonori Ito, Kohji Nakamura, Tamio Oguchi, and M Weinert. Scaled effective on-site Coulomb interaction in the DFT+U method for correlated materials. *Physical Review B*, 97(3):035117, 2018.
- ²⁰Xiaobo Chen, Lei Liu, Peter Y Yu, and Samuel S Mao. Increasing Solar Absorption for Photocatalysis with Black Hydrogenated Titanium Dioxide Nanocrystals. *Science*, 331(6018):746–750, 2011.
- ²¹John C Matsubu, Shuyi Zhang, Leo DeRita, Nebojsa S Marinkovic, Jingguang G Chen, George W Graham, Xiaoqing Pan, and Phillip Christopher. Adsorbate-mediated strong metal-support interactions in oxide-supported Rh catalysts. *Nature chemistry*, 9(2):120–127, 2017.
- ²²Qing Guo, Chuanyao Zhou, Zhibo Ma, and Xueming Yang. Fundamentals of TiO_2 Photocatalysis: Concepts, Mechanisms, and Challenges. *Advanced Materials*, 31(50):1901997,

- 2019.
- ²³Rui Lang, Xiaorui Du, Yike Huang, Xunzhu Jiang, Qian Zhang, Yalin Guo, Kaipeng Liu, Botao Qiao, Aiqin Wang, and Tao Zhang. Single-Atom Catalysts Based on the Metal-Oxide Interaction. *Chemical reviews*, 120(21):11986–12043, 2020.
- ²⁴Feng Jiao and Peter George Bruce. Mesoporous Crystalline β - MnO_2 a Reversible Positive Electrode for Rechargeable Lithium Batteries. *Advanced Materials*, 19(5):657–660, 2007.
- ²⁵Aurélie Débart, Allan J Paterson, Jianli Bao, and Peter G Bruce. α - MnO_2 Nanowires: A Catalyst for the O_2 Electrode in Rechargeable Lithium Batteries. *Angewandte Chemie International Edition*, 47(24):4521–4524, 2008.
- ²⁶P. Blaha, K. Schwarz, G. K. H. Madsen, D. Kvasnicka, and J. Luitz. *WIEN2k: An Augmented Plane Wave Plus Local Orbitals Program for Calculating Crystal Properties*. Technische Universität Wien, 2001. Austria.
- ²⁷David J. Singh and Lars Nordström. *Planewaves, Pseudopotentials and the LAPW Method*. Springer, Boston, MA, second edition edition, 2005.
- ²⁸G. K. H. Madsen and P. Novák. Charge Order in Magnetite. An LDA+U Study. *Europhysics Letters*, 69(5):777, 2005.
- ²⁹J. P. Perdew, K. Burke, and M. Ernzerhof. Generalized Gradient Approximation Made Simple. *Physical Review Letters*, 77(18):3865–3868, 1996.
- ³⁰J. P. Perdew, K. Burke, and M. Ernzerhof. Perdew, burke, and Ernzerhof Reply:. *Physical Review Letters*, 80(4):891, 1998.
- ³¹V. I. Anisimov, J. Zaanen, and O. K. Andersen. Band Theory and Mott Insulators: Hubbard U Instead of Stoner I. *Physical Review B*, 44:943, 1991.
- ³²V. I. Anisimov and O. Gunnarsson. Density-Functional Calculation of Effective Coulomb Interactions in Metals. *Physical Review B*, 43:7570, 1991.
- ³³Akio Yoshimori. A New type of Antiferromagnetic Structure in the Rutile Type Crystal. *Journal of the Physical Society of Japan*, 14(6):807–821, 1959.
- ³⁴Nobuhiko Ohama and Yoshikazu Hamaguchi. Determination of the exchange integrals in β - mno_2 . *Journal of the Physical Society of Japan*, 30(5):1311–1318, 1971.
- ³⁵M Regulski, R Przeniosło, I Sosnowska, and J-U Hoffmann. Incommensurate magnetic structure of β - MnO_2 . *Physical Review B*, 68(17):172401, 2003.
- ³⁶Cesare Franchini, Raimund Podloucky, Joachim Paier, Martijn Marsman, and Georg Kresse. Ground-state properties of multivalent manganese oxides: Density functional

- and hybrid density functional calculations. *Physical Review B—Condensed Matter and Materials Physics*, 75(19):195128, 2007.
- ³⁷Ruchika Mahajan, Iurii Timrov, Nicola Marzari, and Arti Kashyap. Importance of intersite Hubbard interactions in β - MnO_2 : A first-principles DFT+U+V study. *Physical Review Materials*, 5(10):104402, 2021.
- ³⁸Okan K. Orhan and David D. O’Regan. First-principles Hubbard U and Hund’s J corrected approximate density functional theory predicts an accurate fundamental gap in rutile and anatase TiO_2 . *Physical Review B*, 101:245137, 2020.
- ³⁹G. Mattioli and F. Filippone. Ab Initio Study of the Electronic States Induced by Oxygen Vacancies in Rutile and Anatase TiO_2 . *Physical Review B*, 2008.
- ⁴⁰Zhongnan Xu, Jan Rossmeisl, and John R Kitchin. A Linear Response DFT+ U Study of Trends in the Oxygen Evolution Activity of Transition Metal Rutile Dioxides. *The Journal of Physical Chemistry C*, 119(9):4827–4833, 2015.
- ⁴¹Matteo Farnesi Camellone, Piotr M Kowalski, and Dominik Marx. Ideal, defective, and gold-promoted rutile TiO_2 (110) surfaces interacting with CO , H_2 , and H_2O : Structures, energies, thermodynamics, and dynamics from PBE+ U. *Physical Review B—Condensed Matter and Materials Physics*, 84(3):035413, 2011.
- ⁴²Matteo Cococcioni and Stefano De Gironcoli. Linear response approach to the calculation of the effective interaction parameters in the LDA+U method. *Physical Review B—Condensed Matter and Materials Physics*, 71(3):035105, 2005.
- ⁴³Giuseppe Mattioli, Paola Alippi, Francesco Filippone, Ruggero Caminiti, and Aldo Amore Bonapasta. Deep versus Shallow Behavior of Intrinsic Defects in Rutile and Anatase TiO_2 Polymorphs. *The Journal of Physical Chemistry C*, 114(49):21694–21704, 2010.
- ⁴⁴C Herring. Magnetism g. rado and suhl, h. eds. vol. 4, 1966.
- ⁴⁵I. V. Solovyev and P. H. Dederichs. Ab Initio Calculations of Coulomb U Parameters for Transition-Metal Impurities. *Physical Review B*, 49(10):6736–6740, 1994.
- ⁴⁶Qing Zhao and Heather J Kulik. Where does the density localize in the solid state? divergent behavior for hybrids and dft+ u. *Journal of chemical theory and computation*, 14(2):670–683, 2018.
- ⁴⁷Y Crespo and N Seriani. Electronic and magnetic properties of α - MnO_2 from ab initio calculations. *Physical Review B—Condensed Matter and Materials Physics*, 88(14):144428, 2013.

- ⁴⁸John B Goodenough. Theory of the Role of Covalence in the Perovskite-Type Manganites [La, M (II)] MnO₃. *Physical Review*, 100(2):564, 1955.
- ⁴⁹John B Goodenough. An interpretation of the magnetic properties of the perovskite-type mixed crystals La_{1-x}Sr_xCoO_{3-λ}. *Journal of Physics and Chemistry of Solids*, 6(2-3):287–297, 1958.
- ⁵⁰Junjiro Kanamori. Superexchange interaction and symmetry properties of electron orbitals. *Journal of Physics and Chemistry of Solids*, 10(2-3):87–98, 1959.
- ⁵¹Philip W Anderson. Antiferromagnetism. Theory of Superexchange Interaction. *Physical Review*, 79(2):350, 1950.